Structural and Functional Analysis of Intact Hair Follicles and Pilosebaceous Units by Volumetric Multispectral Optoacoustic Tomography

Steven J. Ford[1,2], Paul L. Bigliardi[3,4], Thomas C.P. Sardella[2], Alexander Urich[2], Neal C. Burton[2], Marcin Kacprowicz[2], Mei Bigliardi[3,4], Malini Olivo[5] and Daniel Razansky[1,6]

Visualizing anatomical and functional features of hair follicle development in their unperturbed environment is key in understanding complex mechanisms of hair pathophysiology and in discovery of novel therapies. Of particular interest is in vivo visualization of the intact pilosebaceous unit, vascularization of the hair bulb, and evaluation of the hair cycle, particularly in humans. Furthermore, noninvasive visualization of the sebaceous glands could offer crucial insight into the pathophysiology of follicle-related diseases and dry or seborrheic skin, in particular by combining in vivo imaging with other phenotyping, genotyping, and microbial analyses. The available imaging techniques are limited in their ability for deep tissue in vivo imaging of hair follicles and lipid-rich sebaceous glands in their entirety without biopsy. We developed a noninvasive, painless, and risk-free volumetric multispectral optoacoustic tomography method for deep tissue three-dimensional visualization of whole hair follicles and surrounding structures with high spatial resolution below 80 μm. Herein we demonstrate on-the-fly assessment of key morphometric parameters of follicles and lipid content as well as functional oxygenation parameters of the associated capillary bed. The ease of handheld operation and versatility of the newly developed approach poise it as an indispensable tool for early diagnosis of disorders of the pilosebaceous unit and surrounding structures, and for monitoring the efficacy of cosmetic and therapeutic interventions.

INTRODUCTION

Visualization of the entire viable hair follicle, including the pilosebaceous unit (PSU) and papilla, is important for characterizing various types of follicular-related disorders, including hair loss (alopecia), acne, folliculitis, keratosis pilaris, and seborrheic or dry skin conditions. Inheritable alopecia is correlated with a number of abnormalities, including hormonal factors [e.g., androgenic, dihydrotestosterone (Sawaya and Price, 1997; Schweikert and Wilson, 1974)] gene transcription factors (e.g., Mediator coactivator (Oda et al., 2012), SOX21 (Kiso et al., 2009)], and other cell signaling pathways [Shh, Wnt, growth factors (Johnstone and Albert, 2002; Malkinson et al., 1993)]. However, exactly how these and other underlying factors are linked to healthy or aberrant morphometry and cycling of the PSU and cause hair thinning and loss still is unclear.

Real-time, three-dimensional (3D), in vivo visualization of the entire, intact PSU could aid in understanding the causes and consequences of various forms of alopecia and follicular diseases. Current methods to examine intact hair follicle viability rely primarily on biopsies, which are unfavorable because of their invasiveness. In addition, fixation and staining solutions may dehydrate the tissue slice and disrupt the overall structure of the PSU, and the hair follicle cannot be used to study the progression of disease or treatment over time. Biopsying also limits information to single time points, yet observations over time can add a new dimension to morphological assessment. Thus, noninvasive imaging approaches are appealing for longitudinal observations of the structures of the PSU. Current imaging methods are restricted by the optical diffusion limit (e.g., in vivo reflectance confocal imaging and optical coherence tomography) and by the spatial resolution (e.g. ultrasound or

[1]Institute for Biological and Medical Imaging (IBMI), Helmholtz Zentrum München, Neuherberg, Germany; [2]iThera Medical GmbH, Munich, Germany; [3]Clinical Research Unit for Skin, Allergy and Regeneration (CRUSAR), Institute of Medical Biology, Agency for Science, Technology and Research, Singapore; [4]National University of Singapore YLL School of Medicine and University Medicine Cluster, Division of Rheumatology, National University Hospital, Singapore; [5]Singapore Bioimaging Consortium (SBIC), Agency for Science, Technology and Research, Singapore; and [6]Faculty of Medicine, Technische Universität München, Munich, Germany

Correspondence: Daniel Razansky, Institute of Biological and Medical Imaging (IBMI), Helmholtz Zentrum München and Technical University of Munich Ingolstädter Landstraße 1D-85764 Neuherberg, Germany. E-mail: dr@tum.de or Paul L. Bigliardi, Clinical Research Unit for Skin, Allergy and Regeneration (CRUSAR), Institute of Medical Biology, A*STAR, 11 Biopolis Way, Helios Building, #01-06/07, 138667, Singapore. E-mail: paul.bigliardi@imb.a-star.edu.sg or Malini Olivo, Singapore Bioimaging Consortium (SBIC), Biomedical Sciences Institutes, 11 Biopolis Way, #02-02 Helios, 138667, Singapore. E-mail: malini_olivo@sbic.a-star.edu.sg

ARTICLE IN PRESS

SJ Ford et al.
Analysis of Intact Pilosebaceous Units by vMSOT

optical coherence tomography), thus limiting the ability of these methods to image pilosebaceous structures found at depth. Recent advances in multiphoton microscopy approaches allow for imaging of labeled follicular cells (Rompolas et al., 2012), but visualization of the PSU is hindered by the effective imaging depth, which is in the range of hundreds of micrometers due to strong light scattering in living tissues.

Limitations of optical microscopy related to light scattering in living tissues can be generally overcome by optoacoustic techniques (Razansky et al., 2012). By detecting pressure waves induced via short laser pulses, optoacoustic methods have recently enabled high-resolution imaging at depths of several millimeters to centimeters (Razansky, 2012; Razansky et al., 2009a; Yao and Wang, 2014), orders of magnitude deeper than modern microscopy. The ability to spatially resolve tissue chromophores provides the added advantage of optoacoustic techniques: multispectral imaging (i.e., images taken at multiple excitation wavelengths) and unmixing allow for visualization of intrinsic tissue chromophores, such as melanin (Krumholz et al., 2011), oxyhemoglobin and deoxyhemoglobin (Laufer et al., 2007; Wang et al., 2003), lipids, and water. The potential of multispectral optoacoustic tomography for functional and molecular imaging is highlighted by the broad range of biological applications, including cardiovascular imaging (Taruttis et al., 2010, 2013), monitoring of organ perfusion and pharmacokinetics (Razansky et al., 2011; Taruttis et al., 2012), targeted studies of inflammation and arthritis (Beziere et al., 2014; Fournelle et al., 2012; Vonnemann et al., 2014), and neuroimaging (Wang et al., 2003, 2006). Recently, the optoacoustic approach has been also applied toward imaging the dermal layers, microvasculature, nevus, and melanoma of the skin (Favazza et al., 2011; Ida et al., 2014; Schwarz et al., 2014; Vionnet et al., 2014).

In this study, we imaged human hair follicles and resolved intrinsic absorbers in the PSU, such as melanin, hemoglobin, and lipid structures in their natural intact in vivo environment by developing a high-resolution volumetric multispectral optoacoustic tomography (vMSOT) platform. vMSOT provided sensitive spatial assessment of melanin in the hair shaft, hemoglobin in blood vessels and dermal papilla, and lipids in the region of sebaceous glands and hypodermal fat, thus resolving key structures of the PSU. Our findings suggest that vMSOT has high potential for clinical and research applications, providing a tool to explore the link between morphologies of intact pilosebaceous structures and molecular mechanisms of hair growth.

RESULTS

Anatomical features as identified in single-wavelength images

Figure 1a shows a schematic of the imaging system, and Figure 1b shows a representative 3D optoacoustic image of a small cluster of hair follicles on the scalp. The entire hair follicle, which extends toward the skin surface from deep within the tissue, can be readily identified in the image. Important morphometric features, such as hair follicle length, were subsequently determined, allowing for a distinction of phases of growth for each hair follicle. Hairs marked as 1 and 2 in Figure 1b had measured shaft lengths of about 3 mm and uniform structure, suggesting these hairs were in the normal growth phase (anagen). Conversely, the hair marked as 3 had a measured shaft length of approximately 2 mm, and the dermal papilla appeared detached from the hair shaft, indicating that this hair may be in the transition or resting phases
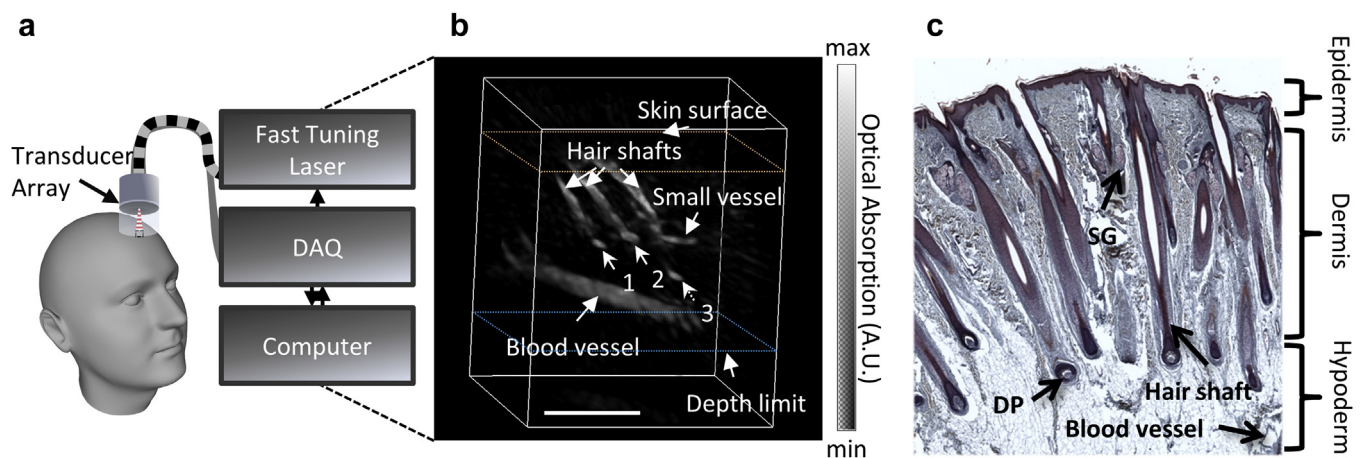

Figure 1. Handheld optoacoustic probe for high-resolution real-time imaging of hair follicles. (**a**) Schematic of the imaging system and approach. The subject is imaged using a 512-element semispherical detector array that captures three-dimensional (3D) multispectral optoacoustic data in real time. The region of interest is illuminated using a pulsed optical parametric oscillator laser capable of fast wavelength tuning in an extended range from 660 to 1300 nm at a rate up to 100 Hz. The data acquisition unit (DAQ) simultaneously digitizes the optoacoustic signals, which are subsequently processed using a graphics processing unit-accelerated image reconstruction code to render 3D images for each laser shot. (**b**) Representative 3D optoacoustic image from healthy volunteer no. 1, demonstrating general physiological structures below the skin surface, including the hair shafts and bulbs, dermal papilla (indicated by numbered arrows), and a deeper, larger blood vessel. Bar = 3 mm. The dermal papilla appear to be detached in the hair marked by arrow 3, suggesting this follicle may be in the catagen or telogen phase, whereas the dermal papillae of the hairs marked by arrows 1 and 2 appear to be attached, suggesting these follicles are in an anagen phase. (**c**) Representative Masson trichrome microscope image (original magnification ×10) from paraffin-embedded scalp hair of a healthy individual. Compared with the optoacoustic images, it reveals similar structures, namely, the dermal papilla (DP), hair shafts and bulbs, and a large subcutaneous blood vessel. The hair bulbs and dermal papilla are located at some places in the subcutaneous fat tissue. Also visible in the histological image are sebaceous glands (SG) in the dermis attached to the upper half of the hair shaft and below the epidermis.

ARTICLE IN PRESS

SJ Ford et al.
Analysis of Intact Pilosebaceous Units by vMSOT

(catagen or telogen). For comparison, Figure 1c depicts corresponding structures as they appear on a typical histological Masson trichrome staining of a normal scalp biopsy. The effective penetration depth of our imaging method can be determined from the images as the deepest resolvable structure in the reconstructed 3D volume. The deepest resolvable structure was a large blood vessel, identified by characteristic hemoglobin absorption (data not shown) and determined to be ∼4.7 mm below the skin surface (indicated by the blue dashed line in Figure 1b).

Supplementary Movie 1 (online) further presents maximal intensity projection (MIP) views recorded at a single wavelength of 850 nm at a frame rate of 20 volumes per second. For this, the probe was scanned across a small region on the forehead, starting at the hairline, moved to the vertex, and returned below the hairline focusing on visualization of vessels. A maximum of 16 individual hairs were visible in these datasets (see Supplementary Movie 1, frame 35), imaged on the vertex of the scalp.

Multispectral unmixing for specific chromophores
Linear spectral unmixing of optoacoustic images acquired at multiple wavelengths (for details see Supplementary Materials online) further enhanced specificity in detecting various tissue chromophores in the PSU by using their known absorption profiles (Figure 2a). Results from the linear unmixing of a single hair follicle are shown in Figure 2b, allowing for a unique and robust separation of the unmixed chromophores. The structures of the same single PSU on the scalp are shown in detail in Figure 3, and unmixing results of a cluster of PSUs on the hand is further shown in Figure 4. The abilities of vMSOT to resolve these key chromophores with high contrast and spatial accuracy are additionally highlighted in Supplementary Movie 2 (online) showing rotational view of the unmixed 3D reconstruction. Thus, several key structural components of the PSUs were delineated by the unmixing method, making possible the visualization of blood perfusion (i.e., unmixed hemoglobin signal) in the dermal papilla, surrounding dermis, and subcutaneous tissue, as well as evaluation of the relative level of blood oxygenation in these structures. In addition, spectrally unmixed images allowed for structural analyses of the dermal papilla and of the lipid- and melanin-rich structures surrounding the hair follicle.

Oxygenation of root capillary bed
As indicated in Figure 3, the root structure of the hair follicle on the scalp showed a point of high oxyhemoglobin signal, as was consistent across all the scans taken from the scalp (data not shown). This suggests that the dermal papilla is highly perfused and thus likely to be in the healthy growth (anagen) phase (Mecklenburg et al., 2000). The relative saturation of oxygenated hemoglobin (sO_2) around the dermal papilla, calculated as the ratio between the oxygenated and total hemoglobin, was estimated to be approximately 99% for this particular hair follicle.

Volume analysis of lipid structures
Unmixed images revealed an elliptical structure displaying a strong lipid signal near a hair follicle imaged on the scalp (Figure 3). Major and minor axes of the ellipsoid were
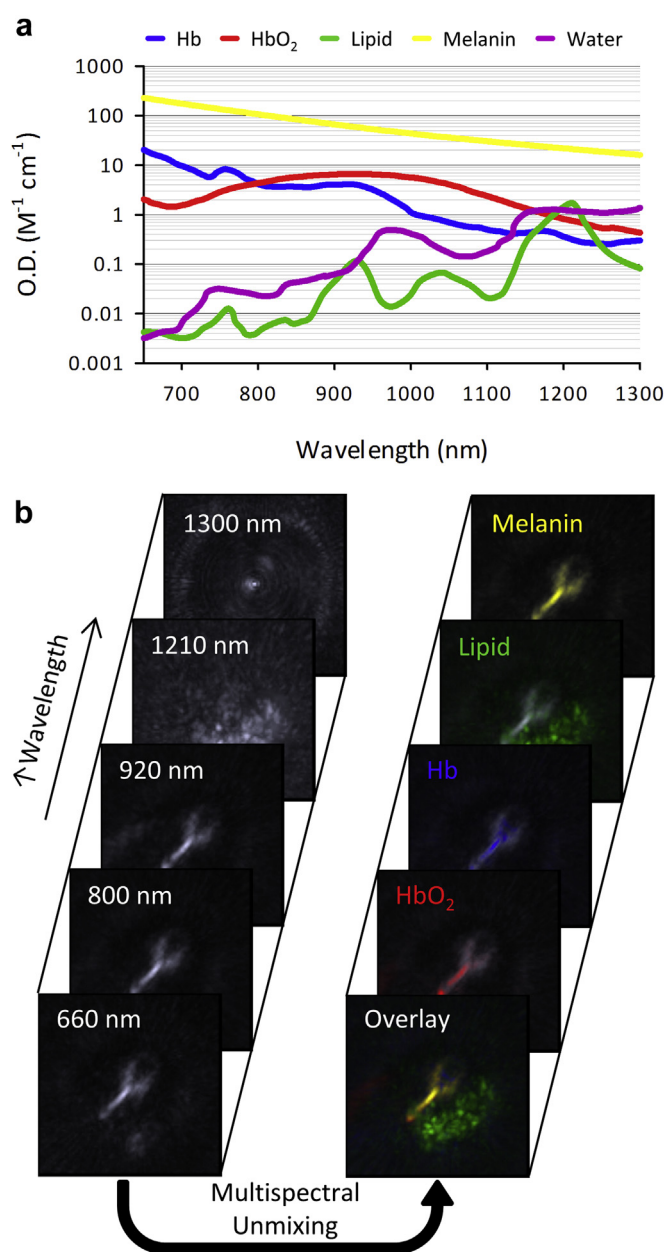

Figure 2. The multispectral imaging approach. (**a**) Images are collected at a range of wavelengths, chosen based on the shown absorption profiles of the chromophores of interest. (**b**) Optoacoustic images acquired at the multiple wavelengths allow for a linear unmixing of the data on a per voxel basis and accurate localization and quantification of the relative contribution of each chromophore. Hb, deoxygenated hemoglobin; HbO_2, oxygenated hemoglobin; O.D., optical density.

estimated to be 4.3, 2.5, and 3.4 mm, which gave an overall lipid volume of 153 μl. Because of its superficial location around the hair follicle, near the upper half of the hair shaft and close to the skin surface, much of this lipid signal is assumed to comprise sebaceous glands surrounding the PSU for this hair shaft. The dense and deep lipid structures close to the blood vessels identified in the hand (Figure 4) were more dispersed and may correlate to lipids from subcutaneous fat.

Noninvasive measurements of entire hair follicle
Measurements were made from the unmixed melanin images and compared between three follicles found on the head
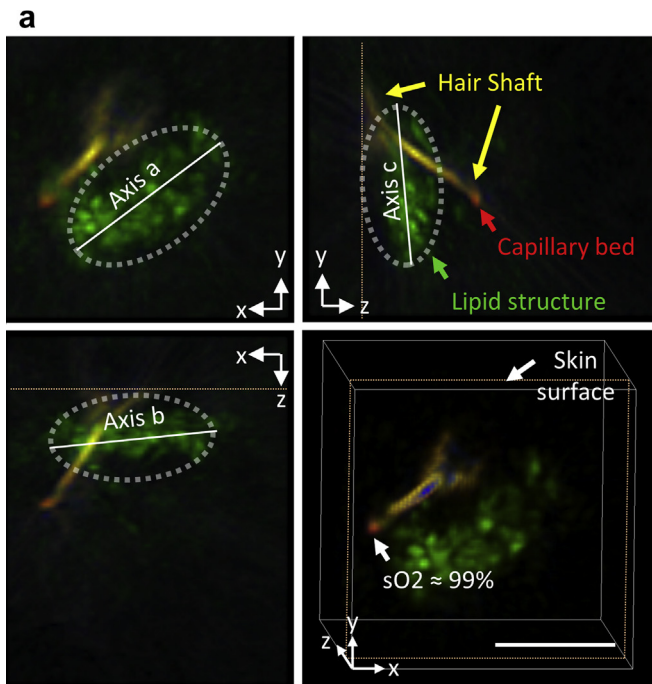
Figure 3. Single pilosebaceous unit imaged on the forehead. (a) Unmixed images of a single hair on the scalp of healthy volunteer no. 2. Multispectral unmixing allowed for visualization of the single hair at depth and revealed an ellipsoid-like lipid structure near the hair shaft. The dimensions of the lipid content were calculated along three axes shown in the orthogonal view in panel a (axis a = 4.3 mm, axis b = 2.5 mm, axis c = 3.4 mm), giving an estimated elliptical lipid volume of 153 μl. Inset frame shows a three-dimensional representation of the unmixed data. Bar = 3 mm. Of particular interest is that the follicle bulb shows a high level of oxygenation, presumably corresponding to the highly oxygenated capillary bed feeding the follicle. Colors reflect the contribution of each of the unmixed chromophores as follows: gray = optoacoustic signal at 800 nm; blue = deoxyhemoglobin; red = oxyhemoglobin; green = lipid; yellow = melanin. (b) Measurements of shaft thickness of three hairs at 10 different depths, starting at the dermal papilla and ending at the skin surface, from the same volunteer. sO_2, saturation of oxygenated hemoglobin relative total hemoglobin content.

Figure 4. A cluster of pilosebaceous units imaged on the hand. (a) Unmixed images of the hand of healthy volunteer no. 2 in a region where both a mole (melanocyte deposit) and hairs are seen. The unmixed signal shows a strong lipid content, as well as strong melanin content, correlating to melanin concentrated in the hairs and mole. The lipid content was dispersed around the hairs deep under the skin surface, as can be seen in the orthogonal and three-dimensional views of the hair. Bar = 3 mm. (b) Measurements of shaft thickness of three hairs at 10 different depths, starting at the dermal papilla and ending at the skin surface, from the same volunteer.

and three on the hand of one healthy volunteer. The lengths of the hair follicles were longer on the scalp than on the hand ($P < 0.05$), measuring approximately 3.16 ± 0.06 mm on the head (Figure 3) compared to 2.19 ± 0.23 mm on the hand (Figure 4). Likewise, the volumes of the hair shaft and bulb
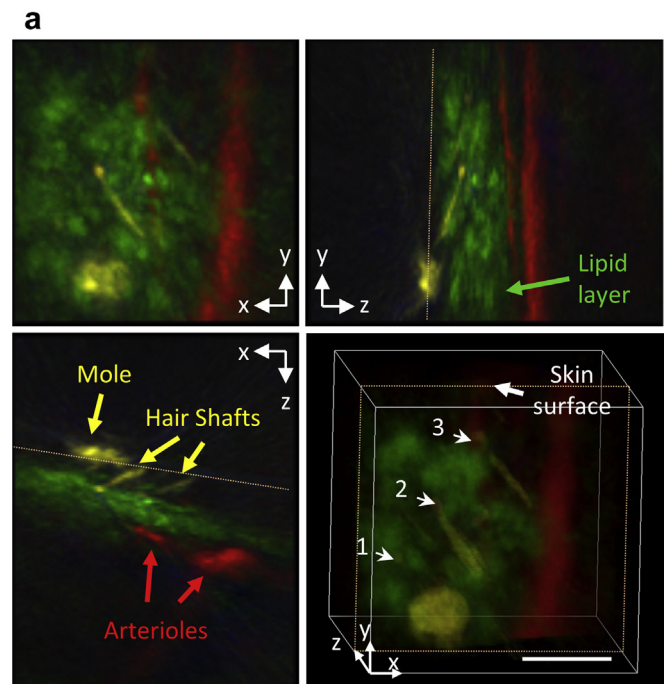
were greater on the scalp ($P < 0.05$), measuring approximately 0.28 ± 0.06 mm^3 on the head (Figure 3) compared to 0.09 ± 0.03 mm^3 on the hand (Figure 4). The thicknesses of the entire hair shafts were also determined on both the scalp (Figure 3b) and the hand (Figure 4b), along the depth of each hair. In general, hair was thicker on the scalp compared to the hand ($P < 0.05$), and all hairs were thickest at the level of the hair bulb and papilla and became thinner toward the skin surface. These findings fit well with what is expected because terminal hairs on scalp are expected to be longer, thicker, and deeper compared to terminal hairs on the hand, where fewer
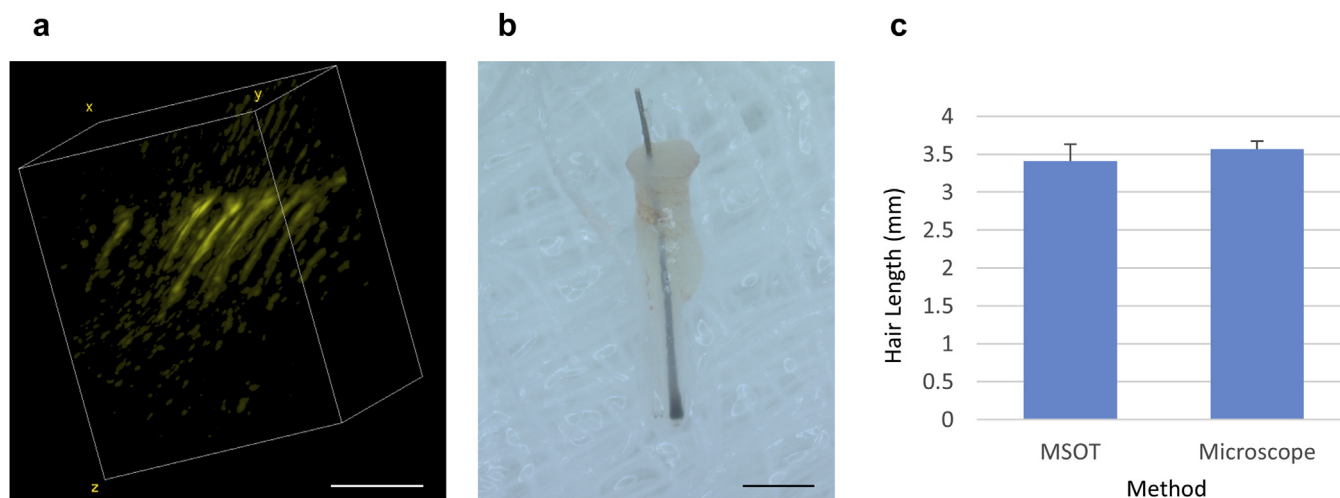
ARTICLE IN PRESS

SJ Ford et al.
Analysis of Intact Pilosebaceous Units by vMSOT

a

b

c

Figure 5. Validation of hair shaft dimensions against microscope observations of an extracted follicular unit. (**a**) Volumetric multispectral optoacoustic tomography (vMSOT) scan from the scalp (vertex) area of healthy volunteer no. 3. Bar = 3 mm. (**b**) Representative microscope image from an extracted follicular unit of the same volunteer (punch diameter 1.1mm) in the same region of vMSOT imaging. Bar = 1 mm. (**c**) Comparison between the noninvasive vMSOT estimations and the microscopic measurements of the extracted hairs. Values represent the mean value + the standard error of the mean from several hairs (MSOT, n = 10; microscope, n = 7). No statistical difference was found between the two length estimations.

androgenic receptors are expected in the dermal papilla (Randall, 2008; Randall et al., 1991).

Follicle dimension estimations by vMSOT were further compared to microscopy of extracted hair follicle units. The representative analysis shown in Figure 5 demonstrates a good agreement between the hair length measured non-invasively by vMSOT and by microscopic validation in the corresponding follicular unit extraction.

Quantification of melanin in different hair types

Melanin content from volunteers with black, gray, and blonde hairs was estimated from the unmixed melanin signal in each respective scan. Plotted on the same scale, melanin content decreases in the vMSOT images when looking at black to gray to blonde hair types (Figure 6a–c), in congruence with the corresponding color photographs (Figure 6d–f). Overall melanin concentration, assessed by averaging the melanin content in the entire image, was highest in black then in gray and blonde hair types (Figure 6g). Removing voxels outside of the hair shafts also revealed that melanin concentrations specifically localized in the hair shafts was highest in the black hair type, followed by gray and then blonde hair types (Figure 6h).

DISCUSSION

In this study, we developed a technique to measure the structural and physiological features of intact hair follicles using a handheld vMSOT, that to our knowledge has not been previously reported. This imaging paradigm allows for high-resolution, label-free 3D visualization of the structures of the PSU at imaging depths beyond several millimeters. Other optical methods, such as reflectance confocal microscopy, can provide submicrometer resolution images of the skin, but its imaging depth is limited to several hundreds of microns (Calzavara-Pinton et al., 2008). Optical coherence tomography is another optical method of skin imaging that offers resolution on the order of tens of micrometers at depths up to

2 mm (Welzel et al., 1997); however, this is not deep enough to view the dermal papilla at depths over 3 mm. Furthermore, the structural contrast of optical coherence tomography does not provide spectroscopic differentiation between different tissue chromophores. Thus, for imaging of structures of the hair shaft, which is on the order of hundreds of micrometers in width and several millimeters in depth, vMSOT provides an optimal combination of imaging resolution and penetration depth.

Single-wavelength images allow for visualization of the intact PSUs and illustrate the potential for vMSOT to evaluate key morphometric parameters of the hair follicle. Follicular growth phase (anagen, telogen/catagen) was suggested based on the structural characteristics in single-wavelength images; however, growth phase would require validation using histopathology or tracking follicular growth over time in the same hair follicles. Although histopathology could not be performed on the volunteers imaged, structures observed by vMSOT (i.e., hair shaft, dermal papilla, etc.) correlated with what is expected in a typical histological slice and biopsy of the PSU (Jimenez et al., 2011). Furthermore, the noninvasive vMSOT-based hair length measurements correlated well with the microscopic measurements made on the extracted hair (Figure 5). Because the vMSOT method does not require extraction of the follicular unit, the morphology and growth phase of an individual intact hair follicle can be potentially monitored over several growth cycles. Morphological information of the intact follicle would be of high value in longitudinal studies of hair pathophysiology and the response of the hair follicle cycle to treatments and environmental factors (e.g., chemotherapy).

Unmixing of tissue chromophores increased the specificity in visualizing key features, including melanin-containing structures (e.g., moles, hair bulb and shafts), as well as lipid-containing structures (e.g., sebaceous glands and/or subcutaneous fat). Although the spectrum used in the unmixing algorithm was not specific to sebum, the measured
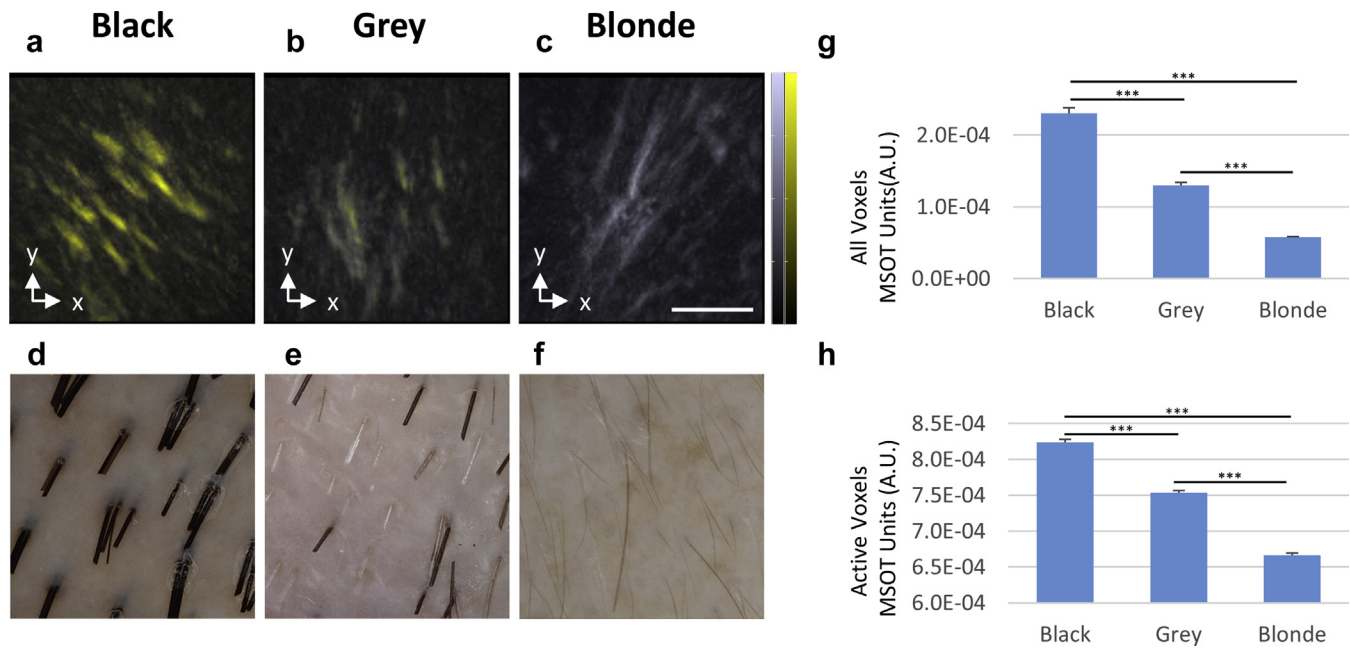
ARTICLE IN PRESS

SJ Ford et al.
Analysis of Intact Pilosebaceous Units by vMSOT

Figure 6. Comparison of melanin signal in hair types having three different pigmentations. Unmixed melanin is overlain on single wavelength images (background) at 660 nm for volunteers with (**a**) black hair type—volunteer no. 4, (**b**) gray hair type—volunteer no. 3, or (**c**) blonde hair type—volunteer no. 5. Bar = 3 mm. Gray and yellow color bars represent respective background signal at 660 nm and unmixed melanin signals, respectively. (**d**–**f**) Corresponding high-resolution photographs of imaged volunteers are shown. (**g**) Average melanin in the entire image shows higher signal in the black hair phenotype. (**h**) Thresholding to include only voxels in hair (active voxels) shows a similar trend in which melanin is the highest in black hairs and lowest in blonde hairs. ***$P < 0.001$. Values represent the mean value + the standard error of the mean from several scans on each volunteer (black, n = 10; gray, n = 7; blonde, n = 21).

spectra, particularly the peak absorbance at ~1210 nm, were similar to what was reported previously for fatty tissue and sebum (Anderson et al., 2006; Sakamoto et al., 2012). Lipid content produced by the sebaceous glands of the PSUs is important for follicular health (Zouboulis et al., 2014), and is known to have a unique composition of fatty acids in normal sebum analytes (Zouboulis et al., 2008). In future studies, these spectra may allow for more accurate unmixing of sebaceous glands and morphometric analyses of in studies of the PSU.

The multispectral approach further allowed for physiological estimation of perfusion and blood oxygenation of the follicle bulb and the surrounding capillary bed. Perfusion and relative oxygenation are viewed as important potential markers of healthy hair growth, as perfusion correlates to the phase of the hair cycle (Mecklenburg et al., 2000, Stenn and Paus, 2001) and may help characterize efficacies of potential therapies. Although errors associated with wavelength-dependent light attenuation are inherent to MSOT, <10% error is expected in the estimated sO_2 values at the relatively shallow ~3mm depth of the dermal papilla (Deán-Ben et al., 2014; Roman et al., 2014). vMSOT also provides the unique advantage of high spatial sensitivity in the sO_2 estimations compared to pulse oximetry, which only provides integrated (bulk) measurements that lack spatial resolution. Compared to needle-type oximeters, vMSOT also offers an advantage of noninvasiveness, fast acquisition of 3D data, and inherent spatial registration of the sO_2 measurements with other (i.e. non-hemoglobin) anatomical features in the images.

Another unique finding was the ability to quantify unmixed melanin signal and to use this to characterize hairs of different color. The unmixed melanin component showed

relatively high signal in the hair shaft compared to the skin and surrounding tissue of the epidermis, especially in darker hair types in which the relative melanin concentration in the hair shaft was highest (Figure 6). This unique assignment demonstrated confidence in vMSOT to resolve melanin-rich structures and sensitivity to differentiate chromophore content. This capacity potentially can be extended to investigating differences in lipid characteristics, for example, in cases of pathophysiological conditions in which lipid structures and function in the PSU may vary.

Although this study shows promise for vMSOT to characterize structures of the PSU after multispectral unmixing, validation in pathophysiological conditions remains the biggest limitation of this study, which only focused on studying human volunteers. First, histopathology would be valuable in future clinical studies in which changes in morphometric parameters need to be validated using a recognized method. Second, validation of the transition of a single follicle from anagen to catagen to telogen could be done over a longitudinal scan but may require months or years to visualize for one hair follicle. Although histopathology may provide adequate validation for static images to compare hair follicle states, intact longitudinal studies would be of higher value in monitoring treatments targeting the reversal of telogen to anagen in alopecia patients.

In conclusion, these studies highlight the capabilities of optoacoustic imaging in visualizing the PSU and hair follicle structure. Parameters related to perfusion (i.e., sO_2) and root structure (i.e., length, volume) may be useful in future studies to determine phase characteristics of the follicle, and thus offer parameters for in vivo testing of the mechanisms and potential treatments of alopecia. Refinement of lipid

ARTICLE IN PRESS

SJ Ford et al.
Analysis of Intact Pilosebaceous Units by vMSOT

unmixing will further allow for determination of whether a disease or treatment impacts sebaceous gland function. Collectively, these findings offer a previously unreported approach to characterizing the structure and status of the PSU and to studies of potential treatments.

MATERIALS AND METHODS
Experimental system
An illustration of the handheld system components is shown in Figure 1a. Healthy volunteers were imaged on the head or hand, where hairs were shaved before the imaging session. Optoacoustic signals were generated in the scalp or hand of healthy volunteers using a pulsed laser system capable of generating nanosecond pulses at a rate of up to 100 Hz and fast wavelength tuning in the range between 660 and 1300 nm on a per pulse basis (Innolas Laser GmbH, Krailling, Germany). The resulting optoacoustic responses were measured using a custom-made handheld ultrasound detection array, consisting of 512 detection elements arranged in a semi-spherical geometry covering a solid angle of approximately 140° (Imasonic, Voray-sur-l'Ognon, France). The individual elements provided broad detection bandwidth of 70% around the central frequency of 10 MHz, corresponding to diffraction-limited spatial resolution of 75 μm (see Supplementary Figure S1 online). Data were acquired using a custom-built data acquisition unit (Falkenstein Mikrosysteme GmbH, Taufkirchen, Germany), which is triggered by the laser pulses and simultaneously acquires signals from the individual detection elements at a rate of 40 megasamples per second. Uniform ultrasound coupling between the subject and detector was provided by filling a custom-made coupling chamber with heavy water (D_2O) to reduce absorption of light by water at long wavelengths. A thin, optically and acoustically transparent, water-tight polyethylene membrane was fixed to the edges of the coupling chamber, allowing for easy replacement and sterile use between imaging sessions.

System characterization
The sensitivity of the newly designed 512-element detector array was determined according to the previously described procedures (Deán-Ben and Razansky, 2013). In brief, a point source generating a spherical pressure wave was modeled for a set of different positions in the field of view of the detector array. The summed responses for all of the individual elements generated a sensitivity map as shown in Supplementary Figure S2 (online), repeated for three different frequencies, namely, 5, 10, and 15 MHz. Supplementary Figure S1a shows the average impulse response of the individual detector elements measured using a black polyethylene microsphere (50-μm diameter) as a point emitter. Supplementary Figure S1b–d shows the frequency profile of the impulse response, the full width at half-maximum of the combined sensitivity field, and the respective spatial resolution of the spherical array.

Study population
A total of seven healthy, adult male volunteers of European and East Asian ethnicities (skin types IV or less on the Fitzpatrick scale, ethics approval DSRB 2014/00677) were imaged for this study, with ages ranging from 30 to 50 years. Each volunteer was imaged on the scalp and some on the hand to generate the images provided in the article. Volunteers were imaged in compliance with institutional approval at the respective sites, and they provided informed and written consent.

Data processing
Image reconstruction was performed using a 3D back-projection algorithm, as described in detail by Xu and Wang (2005). Opto-acoustic signals were used to reconstruct images within a volume of 7.5 × 7.5 mm and 9-mm depth with an isotropic resolution of 75 μm per voxel. Reconstruction was implemented on a graphics processing unit (Deán-Ben et al., 2013), allowing for near-video rate volumetric image rendering up to 20 Hz. A representative 3D optoacoustic image acquired from the scalp is shown in Figure 1b.

Linear unmixing of multispectral images revealed the spatial distribution of the various tissue chromophores (Razansky et al., 2007, 2009a, 2009b). Volumetric images were acquired at several wavelengths correlating to key spectral features of the chromophores expected within the imaged tissue. In this study, we assumed the following chromophores to have significant contributions to light absorption in the wavelength range supported by the laser: hemoglobin, oxyhemoglobin, lipid, melanin, and water. The spectrum for each chromophore was modeled based on the empirically derived parameters as follows: hemoglobin (Kuenstner et al., 1997; Roggan et al., 1999), melanin (Wolbarsht et al., 1981), lipid (Tsai et al., 2001; Veen et al., 2005), water (Tsai et al., 2001). Distribution of the chromophores was subsequently retrieved by a linear inversion scheme on a per voxel basis using the known molar extinction coefficient spectra of the chromophores of interest (Figure 2a).

Determination of physiological parameters
After spectral unmixing, further analysis of the components was performed to determine key physiological parameters, including lipid and hair follicle dimensions, and relative oxygenation of the capillary beds feeding the hair follicle root. The latter was calculated as the ratio of the oxyhemoglobin by total hemoglobin content (Laufer et al., 2007; Wang et al., 2006) as follows:

$$sO_2 = \frac{AU_{HbO2}}{AU_{Hb} + AU_{HbO2}}$$

Where AU_{HbO2} is the average MSOT absorbance units from the unmixed oxyhemoglobin component, and AU_{Hb} is the average MSOT absorbance units from the unmixed deoxyhemoglobin component. An area of ~300 × 300 × 450 μm in the image was analyzed based on highly oxygenated and deoxygenated hemoglobin, correlating to subresolution capillary perfusion in the dermal papilla.

An ellipsoid was hand fitted to the lipid structure in Figure 3 in order to determine lipid volume. Hair follicle dimensions and volumes were determined by 3D segmentation of the individual hairs using Amira (FEI Visualization Sciences Group, Mérignac Cedex, France). Data were then expressed as mean ± standard deviation, and a two-tailed unpaired *t* test was used to determine the statistical difference of hair dimensions measured on the head and on the hand.

Analyses of melanin content in hair shafts
Hair types of varying pigmentation (black, gray, and blonde) were imaged, and all tissue components were unmixed. The mean melanin content was determined by averaging the unmixed melanin signal for all voxels in the reconstructed volume. Because overall melanin signal depends on many factors (skin color, number of hairs in imaging view, concentration of melanin in hair), we sought to isolate the concentration in hair shafts by applying a threshold to the melanin channel for further analyses. This threshold was determined

ARTICLE IN PRESS

SJ Ford et al.
Analysis of Intact Pilosebaceous Units by vMSOT

by averaging the maximal voxel values for melanin found in the reconstructed volumes above the skin lines and below dermal papilla in the datasets analyzed (i.e., where only noise is expected), leaving only active voxels where the melanin signal significantly exceeds the noise levels. The average of these voxel values was then calculated to determine the mean melanin value only in the active voxels of the image, thus giving an approximation of average melanin content in the hair shaft. A two-tailed, unpaired t test was used to determine statistical differences in the measured melanin content between the imaged groups.

SUPPLEMENTARY MATERIAL

Supplementary material is linked to the online version of the paper at www.jidonline.org, and at http://dx.doi.org/10.1016/j.jid.2015.09.001.

REFERENCES

Anderson RR, Farinelli W, Laubach H, Manstein D, Yaroslavsky AN, Gubeli J 3rd, et al. Selective photothermolysis of lipid-rich tissues: a free electron laser study. Lasers Surg Med 2006;38:913—9.

Beziere N, von Schacky C, Kosanke Y, Kimm M, Nunes A, Licha K, et al. Optoacoustic imaging and staging of inflammation in a murine model of arthritis. Arthritis Rheumatol 2014;66:2071—8.

Calzavara-Pinton P, Longo C, Venturini M, et al. Reflectance confocal microscopy for in vivo skin imaging. Photochem Photobiol 2008;84:1421—30.

Deán-Ben XL, Razansky D. Functional optoacoustic human angiography with handheld video rate three dimensional scanner. Photoacoustics 2013;1:68—73.

Deán-Ben XL, Bay E, Razansky D. Functional optoacoustic imaging of moving objects using microsecond-delay acquisition of multispectral three-dimensional tomographic data. Sci Rep 2014;4:5878.

Deán-Ben XL, Ozbek A, Razansky D. Volumetric real-time tracking of peripheral human vasculature with GPU-accelerated three-dimensional optoacoustic tomography. IEEE Trans Med Imaging 2013;32:2050—5.

Favazza CP, Jassim O, Cornelius LA, Wang LV. In vivo photoacoustic microscopy of human cutaneous microvasculature and a nevus. J Biomed Opt 2011;16:16015.

Fournelle M, Bost W, Tarner IH, Lehmberg T, Weiß E, Lemor R, et al. Anti-tumor necrosis factor-α antibody-coupled gold nanorods as nanoprobes for molecular optoacoustic imaging in arthritis. Nanomedicine 2012;8:346—54.

Ida T, Kawaguchi Y, Kawauchi S, Iwaya K, Tsuda H, Saitoh D, et al. Real-time photoacoustic imaging system for burn diagnosis. J Biomed Opt 2014;19:086013.

Jimenez F, Izeta A, Poblet E. Morphometric analysis of the human scalp hair follicle: practical implications for the hair transplant surgeon and hair regeneration studies. Dermatol Surg 2011;37:58—64.

Johnstone MA, Albert DM. Prostaglandin-induced hair growth. Surv Ophthalmol 2002;47(Suppl. 1):202.

Kiso M, Tanaka S, Saba R, Matsuda S, Shimizu A, Ohyama M, et al. The disruption of Sox21-mediated hair shaft cuticle differentiation causes cyclic alopecia in mice. Proc Natl Acad Sci U S A 2009;106:9292—7.

Krumholz A, Vanvickle-Chavez SJ, Yao J, Fleming TP, Gillanders WE, Wang LV. Photoacoustic microscopy of tyrosinase reporter gene in vivo. J Biomed Opt 2011;16:80503.

Kuenstner JT, Norris K, Kalasinsky VF. Spectrophotometry of human hemoglobin in the midinfrared region. Biospectroscopy 1997;3:225—32.

Laufer J, Delpy D, Elwell C, Beard P. Quantitative spatially resolved measurement of tissue chromophore concentrations using photoacoustic spectroscopy: application to the measurement of blood oxygenation and haemoglobin concentration. Phys Med Biol 2007;52:141—68.

Malkinson FD, Geng L, Hanson WR. Prostaglandins protect against murine hair injury produced by ionizing radiation or doxorubicin. J Invest Dermatol 1993;101(Suppl 1):135S—7S.

Mecklenburg L, Tobin DJ, Müller-Röver S, Handjiski B, Wendt G, Peters EM, et al. Active hair growth (anagen) is associated with angiogenesis. J Invest Dermatol 2000;114:909—16.

Oda Y, Hu L, Bul V, Elalieh H, Reddy JK, Bikle DD. Coactivator MED1 ablation in keratinocytes results in hair-cycling defects and epidermal alterations. J Invest Dermatol 2012;132:1075—83.

Randall VA. Androgens and hair growth. Dermatol Ther 2008;21:314—28.

Randall VA, Thornton MJ, Hamada K, Redfern CP, Nutbrown M, Ebling FJ, et al. Androgens and the hair follicle. Cultured human dermal papilla cells as a model system. Ann N Y Acad Sci 1991;642:355—75.

Razansky D. Multispectral optoacoustic tomography-volumetric color hearing in real time. IEEE J Sel Top Quantum Electron 2012;18:1234—43.

Razansky D, Baeten J, Ntziachristos V. Sensitivity of molecular target detection by multispectral optoacoustic tomography (MSOT). Med Phys 2009a;36:939—45.

Razansky D, Buehler A, Ntziachristos V. Volumetric real-time multispectral optoacoustic tomography of biomarkers. Nat Protoc 2011;6:1121—9.

Razansky D, Deliolanis NC, Vinegoni C, Ntziachristos V. Deep tissue optical and optoacoustic molecular imaging technologies for preclinical research and drug discovery. Curr Pharm Biotechnol 2012;13:504—22.

Razansky D, Distel M, Vinegoni C, Ma R, Perrimon N, Köster R, et al. Multispectral opto-acoustic tomography of deep-seated fluorescent proteins in vivo. Nat Photonics 2009b;3:412—7.

Razansky D, Vinegoni C, Ntziachristos V. Multispectral photoacoustic imaging of fluorochromes in small animals. Opt Lett 2007;32:2891—3.

Roggan A, Friebel M, Dorschel K, Hahn A, Müller G. Optical properties of circulating human blood in the wavelength range 400—2500 nm. J Biomed Opt 1999;4:36—46.

Roman H, Paul CB, Ben C. Accuracy of approximate inversion schemes in quantitative photoacoustic imaging. Proc SPIE 2014;8943:89435V.

Rompolas P, Deschene ER, Zito G, Gonzalez DG, Saotome I, Haberman AM, et al. Live imaging of stem cell and progeny behaviour in physiological hair-follicle regeneration. Nature 2012;487:496—9.

Sakamoto FH, Doukas AG, Farinelli WA, Tannous Z, Shinn M, Benson S, et al. Selective photothermolysis to target sebaceous glands: theoretical estimation of parameters and preliminary results using a free electron laser. Lasers Surg Med 2012;44:175—83.

Sawaya ME, Price VH. Different levels of 5alpha-reductase type I and II, aromatase, and androgen receptor in hair follicles of women and men with androgenetic alopecia. J Invest Dermatol 1997;109:296—300.

Schwarz M, Omar M, Buehler A, Aguirre J, Ntziachristos V. Implications of ultrasound frequency in optoacoustic mesoscopy of the skin. IEEE Trans Med Imaging 2014;34:672—7.

Schweikert HU, Wilson JD. Regulation of human hair growth by steroid hormones. I. Testosterone metabolism in isolated hairs. J Clin Endocrinol Metab 1974;38:811—9.

Stenn KS, Paus R. Controls of hair follicle cycling. Physiol Rev 2001;81:449—94.

ARTICLE IN PRESS

SJ Ford et al.
Analysis of Intact Pilosebaceous Units by vMSOT

Taruttis A, Herzog E, Razansky D, Ntziachristos V. Real-time imaging of cardiovascular dynamics and circulating gold nanorods with multispectral optoacoustic tomography. Opt Express 2010;18:19592−602.

Taruttis A, Morscher S, Burton NC, Razansky D, Ntziachristos V. Fast multi-spectral optoacoustic tomography (MSOT) for dynamic imaging of pharma-cokinetics and biodistribution in multiple organs. PloS One 2012;7:e30491.

Taruttis A, Wildgruber M, Kosanke K, Beziere N, Licha K, Haag R, et al. Multispectral optoacoustic tomography of myocardial infarction. Photo-acoustics 2013;1:3−8.

Tsai C-L, Chen J-C, Wang W-J. Near-infrared absorption property of biological soft tissue constituents. J Med Biol Eng 2001;21:7−14.

van Veen RL, Sterenborg HJ, Pifferi A, Torricelli A, Chikoidze E, Cubeddu R. Determination of visible near-IR absorption coefficients of mammalian fat using time- and spatially resolved diffuse reflectance and transmission spectroscopy. J Biomed Opt 2005;10:54004.

Vionnet L, Gateau J, Schwarz M, Buehler A, Ermolayev V, Ntziachristos V. 24-MHz scanner for optoacoustic imaging of skin and burn. IEEE Trans Med Imaging 2014;33:535−45.

Vonnemann J, Beziere N, Böttcher C, Riese SB, Kuehne C, Dernedde J, et al. Polyglycerolsulfate functionalized gold nanorods as optoacoustic signal nanoamplifiers for in vivo bioimaging of rheumatoid arthritis. Theranostics 2014;4:629−41.

Wang X, Pang Y, Ku G, Xie X, Stoica G, Wang LV. Noninvasive laser-induced photoacoustic tomography for structural and functional in vivo imaging of the brain. Nat Biotechnol 2003;21:803−6.

Wang X, Xie X, Ku G, Wang LV, Stoica G. Noninvasive imaging of hemo-globin concentration and oxygenation in the rat brain using high-resolution photoacoustic tomography. J Biomed Opt 2006;11:24015.

Welzel J, Lankenau E, Birngruber R, Engelhardt R. Optical coherence to-mography of the human skin. J Am Acad Dermatol 1997;37:958−63.

Wolbarsht ML, Walsh AW, George G. Melanin, a unique biological absorber. Appl Opt 1981;20:2184−6.

Xu M, Wang LV. Universal back-projection algorithm for photoacoustic computed tomography. Phys Rev E Stat Nonlin Soft Matter Phys 2005;71: 16706.

Yao J, Wang LV. Sensitivity of photoacoustic microscopy. Photoacoustics 2014;2:87−101.

Zouboulis CC, Jourdan E, Picardo M. Acne is an inflammatory disease and alterations of sebum composition initiate acne lesions. J Eur Acad Dermatol Venereol 2014;28:527−32.

Zouboulis CC, Schagen S, Alestas T. The sebocyte culture: a model to study the pathophysiology of the sebaceous gland in sebostasis, seborrhoea and acne. Arch Dermatol Res 2008;300:397−413.